Materials Horizons

ROYAL SOCIETY OF CHEMISTRY

COMMUNICATION

View Article Online
View Journal | View Issue



Cite this: *Mater. Horiz.*, 2023, **10**, 4278

Received 3rd April 2023,
Accepted 5th June 2023

DOI: 10.1039/d3mh00503h

rsc.li/materials-horizons



# Charge–orbital synergistic engineering of TM@$Ti_3C_2O_{1-x}B_x$ for highly selective $CO_2$ electrochemical reduction†

Jiahe Peng,[ab] Zuhao Shi,[ab] Jizhou Jiang,[c] Peng Zhang,[d] Jyh-Ping Hsu[e] and Neng Li*[abc]

**Inspired by MXene nanosheets and their regulation of surface functional groups, a series of $Ti_3C_2$-MXene-based single TM atom electrocatalysts with a doped boron (B) atom (TM@$Ti_3C_2O_{2-x}B_x$, TM is V, Cr, Mn, Fe, Co or Ni, $x$ = 0.11) are proposed for achieving a high performance catalytic $CO_2$ reduction reaction ($CO_2$RR). The results reveal that the doped B atom involves in the adsorption reaction of $CO_2$ molecules and CO intermediates in the $CO_2$RR. The TM-to-C and B-to-C π-back bonding contribute to the activation of the $CO_2$ molecules and CO intermediates in the $CO_2$RR. Enough electrons from the single TM atom and B atom occupied orbitals can be injected into the $CO_2$ molecules and *CO intermediates through direct bonding interactions, which effectively alleviates the difficulty of the first hydrogenation reaction step and further helps CO reduction towards $CH_4$. The calculated values of $\Delta G$ for the first hydrogenation reaction and the formation of *CHO on $Ti_3C_2O_{2-x}B_x$ are significantly smaller than those of other single-atom catalysts (SACs). Fe@$Ti_3C_2O_{2-x}B_x$ is found to have the highest electrocatalytic activity with a limiting potential of ~0.40 V and exhibits a high selectivity for obtaining $CH_4$ through the $CO_2$RR compared with the hydrogen evolution reaction. This work is expected to open a research path for engineering the charge–orbital state of the innate atoms of a substrate based on mechanistic insights, which guides the rational design of highly selective MXene-based $CO_2$RR electrocatalysts.**

### New concepts

Although the development of efficient atomic electrocatalysts to resolve activity and selectivity issues of the $CO_2$ reduction reaction ($CO_2$RR) continues to receive increasing attention, it is still challenging. Most of the previous works in this field have primarily focused on TM atoms and introducing a nonmetal atom to modulate the interplay between the TM active centers and multiple intermediates. Herein, we propose a novel mechanism of introducing a boron element, which takes the advantage of charge–orbital synergism to activate the TM atoms of dual atomic electrocatalysts for the $CO_2$RR. The charge and orbital order controlling resulting from the combined effect of the single TM atoms and B atom can effectively activate $CO_2$ molecules and CO intermediates in the $CO_2$RR process. The TM-to-C, and B-to-C π-back bonding contribute to the activation of $CO_2$ molecules and CO intermediates in the $CO_2$RR. Based on this mechanism, we further design a series of TM atoms supported by a monolayer B-doped $Ti_3C_2O_2$ ($Ti_3C_2O_{2-x}B_x$) for the $CO_2$RR. Following a comprehensive screening strategy, Fe@$Ti_3C_2O_{2-x}B_x$ are identified as promising catalysts with high activity and selectivity. Moreover, we identify the valence states of TM as a valid descriptor to evaluate the $CO_2$RR performance on such catalysts, realizing a fast pre-screening of other potential dopants on the MXene-based $CO_2$RR SACs. Our work thus provides a new direction for the rational design of MXene-based dual atomic electrocatalysts.

## 1. Introduction

The rapid economic development and urbanization have already caused a sharp increase in the global concentration of carbon dioxide ($CO_2$).[1,2] The global warming resulting from the excessive consumption of fossil fuels not only poses a serious threat to global economic security but also affects resources, energy, ecology, and food security, among others. It also poses a severe challenge to human survival.[3,4] In an attempt to alleviate the increase in the average global temperature, Paris Climate Change Conference signed the Paris Agreement.[5–7]

[a] *State Key Laboratory of Silicate Materials for Architectures, Wuhan University of Technology, Wuhan 430070, China. E-mail: lineng@whut.edu.cn*
[b] *Shenzhen Research Institute of Wuhan University of Technology, Shenzhen 518000, Guangdong, China*
[c] *School of Chemistry and Environmental Engineering, School of Environmental Ecology and Biological Engineering, Novel Catalytic Materials of Hubei Engineering Research Center, Wuhan Institute of Technology, Wuhan, 430205, China*
[d] *State Center for International Cooperation on Designer Low-Carbon & Environmental Materials (CDLCEM), School of Materials Science and Engineering, Zhengzhou University, Zhengzhou 450001, Henan, China*
[e] *Department of Chemical Engineering, National Taiwan University, Taipei, 10617, China*

† Electronic supplementary information (ESI) available. See DOI: https://doi.org/10.1039/d3mh00503h

The electrochemical reduction of $CO_2$ to produce carbon-based fuels and chemicals has great potential in solving current environmental problems and benefiting the economy of our society.[8,9] However, the high chemical stability of $CO_2$ making it hard to be activated at high conversion rates and selectivity is a crucial issue.[10,11] In addition, the $CO_2$RR pathway includes a chemical dehydration step leading to adsorption of CO,[12–14] which may act as a poison blocking the surface and impeding further protonation steps because of the high desorption energy and a further reduction barrier.[15–17]

In recent years, intense research has been carried out to discover efficient, selective and stable cathode catalysts. Copper-based materials have been widely regarded as efficient cathode materials for the $CO_2$RR, producing diverse products, such as carbon monoxide (CO), formic acid (HCOOH), methanol ($CH_3OH$), methane ($CH_4$), ethanol ($C_2H_5OH$), and ethylene ($C_2H_4$).[18–20] Intense optimization of the catalyst materials and reaction conditions has resulted in significant progress over the past few years.[21,22] Irabien *et al.* found that the $Cu^{II}$ atoms in the HKUST-1 metal–organic framework ($[Cu_3(\mu_6\text{-}C_9H_3O_6)_2]_n$) can promote the electrocatalytic conversion of $CO_2$ to alcohols.[23] The subsequent research studies have reported Cu-based bimetallic electrocatalysts through doping other transition metal atoms to further improve the $CO_2$ conversion performance.[24,25] Therefore, downsizing the metal nanostructures to singly dispersed metal atoms is highly desirable for maximizing the efficiency of catalytically active metal sites. Recently, single-atom catalysts (SACs) containing isolated metal atoms dispersed on solid substrates have attracted significant attention in the field of catalysis.

Single transition metal (TM) atoms anchored on a substrate are widely used as the active sites in the $CO_2$RR.[26,27] The excellent performance of transition metal-based catalysts can be ascribed to their occupied d orbitals, which can donate electrons to the antibonding orbitals of gas molecules.[28–30] Being a nonmetal element, the boron (B) atom in a molecular catalyst with $sp^2$ or $sp^3$ hybridization has exhibited great potential for $N_2$ fixation.[31–33] The B atom also shows the ability to activate $CO_2$ molecules in the $CO_2$RR.[34,35] Tang *et al.* found that the bare edge B on armchair boron nitride nanoribbons is a promising candidate for the catalysis of the $CO_2$RR.[36] In light of the above discussion, the active center of catalysts could be either a single TM atom coordinated by non-metal atoms or a B center. It can be inferred that if B serves as the coordination atom of TM, the active sites with the presence of both B and TM may provide stronger activation capacity.

The results of our previous study indicated that the combined effect of TM and B can effectively and selectively ameliorate the performance of electrochemical $N_2$ reduction.[37] Being an isoelectronic body of $N_2$, CO is likely to be activated owing to the combined effect of TM and B atoms. Liu *et al.* successfully fabricated single atomic Fe sites anchored on B and N co-doped carbon (Fe-SA/BNC), which showed excellent $CO_2$RR activity, achieving the highest faradaic efficiency of ~94% at −0.7 V compared with RHE.[38] However, there is a lack of an in-depth discussion on the mechanisms of $CO_2$ activation. A detailed understanding of these mechanisms at the atomic scale is of great importance for clarifying the synergistic effect between TM and B atoms that contributes to the $CO_2$RR. This is beneficial to developing a suitable catalyst with a high catalytic selectivity for the $CO_2$RR.

In addition to the active center, the choice of substrate is another significant factor that can influence SACs' performance.[39,40] MXenes (*e.g.*, $Ti_3C_2T_x$, $Ti_2CT_x$ and $Mo_2CT_x$), having a general formula of $M_{n+1}X_nT_x$ ($n$ = 1 to 4) with M, X, and $T_x$ being the early transition metals, C or N, and the surface functional groups (usually as –O, –OH or –F), respectively,[41,42] have been considered as potential substrates for various applications,[43,44] especially in the field of SACs.[45–47] Compared with other supports (*e.g.*, doped graphene, $MoS_2$, and g-$C_3N_4$), MXenes have not only the highest metallic conductivity but also abundant surface functional groups for anchoring firmly single atoms.[48] Recently, MXenes have been widely used as the substrates of SACs for the $CO_2$RR.[49] Zhao *et al.* have successfully demonstrated that a Pt@$Ti_3C_2T_x$-based SAC could readily capture $CO_2$ or aniline, yielding value-added amides with a high conversion and selectivity.[50] The subsequent study of Yang *et al.* has produced single atom Cu-immobilized $Ti_3C_2T_x$ for an electrocatalytic $CO_2$RR to produce methanol with a high faradaic efficiency of 59.1%.[51] However, relevant theoretical analyses of the role of B in the MXene-based SACs' $CO_2$RR are very limited. The SACs of single atoms fixed on the $Ti_3C_2T_x$ mixed functional group surface have been successfully synthesized experimentally.[52,53]

In particular, the B atom has been successfully introduced into $Ti_3C_2T_x$ to replace the O functional group on its surface[54] and the single Ru atom anchored on the B-doped $Ti_3C_2T_x$ exhibited outstanding performance for the hydrogen evolution reaction (HER).[55] Relevant reported results provide valuable information for studying the synergistic effect of TM and B atoms on the $CO_2$RR performance of $Ti_3C_2T_x$-based SACs. Our previous theoretical analysis also showed that the $CO_2$RR performance of MXene-based SACs can be efficiently improved through controlling of functional groups.[56] It suggests that an in-depth study on the performance of the $CO_2$RR through

**Neng Li**

*Congratulations on the 10th anniversary and best wishes to Materials Horizons. Our first paper was published in Materials Horizons, and then chosen as the outstanding paper in the in 2018, and selected as "highlighting the members of the Materials Horizons Advisory Board" in 2021. The best way to express our gratitude is to continue to interact closely with the community, and report our significant research advances, such as novel materials, and new reaction mechanisms. We are proud to have solid and excellent cooperation with such an esteemed journal. Here's to another decade, we would like to further contribute this esteemed journal.*

controlling of MXene-based SACs with a mixed functional group surface is necessary. Therefore, we discuss in this study the feasibility of anchoring low cost 3d single TM (TM is V, Cr, Mn, Fe, Co or Ni) atoms on the $Ti_3C_2T_x$'s surface groups as a mixture of B and O ($Ti_3C_2O_{2-x}B_x$) to explore the synergistic effect of TM and B atoms on $Ti_3C_2T_x$-based SACs for the $CO_2$RR. The analysis is based on DFT calculations.

As expected, the results of our computation show that the combined effect of single TM atoms and B atom markedly activated $CO_2$ molecules and CO intermediates after adsorption. This can be attributed to the injection of adequate charge from the occupied p and d orbitals of B and TM, respectively. In addition, the introduction of the B atom into surface groups can significantly enhance the single atom anchoring capacity. The adsorbed $CO_2$ can be further reduced to $CH_4$ on the Fe@$Ti_3C_2O_{2-x}B_x$ SAC with a rather low overpotential of 0.40 eV. The stability of TM@$Ti_3C_2O_{2-x}B_x$ is systematically evaluated, and the results obtained reveal that the designed catalyst can be synthesized promisingly.

## 2. Computational details

All calculations were performed on the Vienna *ab initio* simulation package (VASP).[57] The Perdew–Burke–Ernzerhof (PBE) functional in the generalized gradient approximation (GGA) was used to express electron exchange correlation[58] and a projector augmented wave (PAW) method was applied to describe the pseudo-potentials.[59] Dispersion-corrected DFT-D3 schemes were employed to describe possible van der Waals (VDW) interactions.[60] The energy cut-off for the plane-wave basis was set at 450 eV. All configurations were based on a $3 \times 3 \times 1$ supercell of $Ti_3C_2T_x$ with a vacuum layer larger than 20 Å in the $z$ direction to prevent the interaction between periodic images. The Brillouin zone in reciprocal space was sampled using the Monkhorst–Pack scheme with $5 \times 5 \times 1$ $k$-point grids for geometry optimization and electronic structure calculations.

All structures were fully relaxed until the forces became smaller than 0.01 eV Å$^{-1}$; the convergence threshold in electronic relaxation was set at $10^{-5}$ eV using the conjugate gradient algorithm. The atomic charge was calculated through Bader's charge population analysis.[61] The atomic structures were analyzed using the VESTA code.[62] The effect of water was considered using the VASPsol code.[63–65] The stability of catalysts was evaluated using *ab initio* molecular dynamics (AIMD) simulations carried out by placing MXene in a vacuum or liquid water and lasted for 10.0 ps with a time step of 1 fs in the *NVT* ensemble.

The binding energy ($E_b$) and cohesive energy ($E_c$) of the transition metals on $Ti_3C_2T_x$ can be evaluated using

$$E_b = E_{TM-MX} - E_{MX} - E_{TM} \quad (1)$$

$$E_c = E_{(TMbulk)}/N - E_{TM}, \quad (2)$$

where $E_{TM-MX}$, $E_{MX}$, and $E_{TM}$ are the total energies of $Ti_3C_2T_x$ with and without transition metals and the isolated transition metals, respectively.[66] $E_{(TMbulk)}$ and N are the energy of the bulk crystal unit cell of the corresponding transition metals and the number of atoms in the unit cell, respectively. The adsorption energy ($\Delta E_{ad}$) of the different intermediates can be calculated using

$$\Delta E_{ad} = E_{X^*} - E_* - E_X, \quad (3)$$

where $E_{X^*}$, $E_*$, and $E_X$ represent the energies of the total system after adsorption, the catalyst, and the adsorbates, respectively.[67]

A computational hydrogen electrode (CHE) model proposed by Nørskov *et al.*[68] was used to calculate the Gibbs free energy ($G$) of the reaction for the $CO_2$RR elementary steps involving ($H^+ + e^-$) pair transfer. In the CHE model, $H^+ + e^- \rightleftharpoons 1/2H_2$ (g) is in equilibrium with gaseous $H_2$ at 0 V *vs.* the reversible hydrogen electrode (RHE) for all pH values at 1 bar of $H_2$ pressure. The Gibbs free energy of each elementary step was calculated at 298.15 K using the following eqn (4):

$$G = E + ZPE + \int C_P dT - TS + G_{pH} \quad (4)$$

where $E$ is the total energy and $T$ is the temperature. ZPE, $\int C_P dT$, and $TS$ are the zero-point energy, the enthalpy changes from 0 to $T$ K contributed by molecular vibrations, and the entropy correction based on the calculated vibrational frequencies, respectively. $G_{pH}$ represents the free energy correction for pH, defined as $G_{pH} = -k_B T \ln[H^+] = k_B T \ln 10 \times pH$, where $k_B$ is the Boltzmann constant.

In this work, the pH value was set at 0 for strongly acidic conditions.[68] The dependence of the potential ($U$) on the RHE required for each protonation step is expressed as $U = -\Delta G/e$, where $\Delta G$ is the free energy change along each $CO_2$RR pathway. The limiting potential ($U_L$) was obtained from the maximum $\Delta G(\Delta G_{max})$ of each elementary step. Since the Gibbs free energy of the $O_2$, CO, and $CO_2$ molecules in a gas-phase species cannot be calculated precisely using conventional PBE exchange–correlation function,[14,69] the free energy of the experimental thermodynamic data was used as a ref. 70 and 71. The free energy of liquid-phase molecules ($H_2O$ and $CH_3OH$) was calculated by considering them as an ideal gas and using their corresponding vapor fugacity ($f$) at $\mu_{(liquid)} = \mu_{(vapor)}$.[14]

## 3. Results and discussion

### 3.1. Stability of single atoms embedded on $Ti_3C_2O_{2-x}B_x$

The diffusion and aggregation of the dispersed single atoms on a support can lower the activity and durability of SACs, whereas $Ti_3C_2T_x$ can capture and stabilize the heteroatom effectively through creating tight bonds between the TM atoms and surface groups. In general, the hollow position consisting of three oxygen groups is the main site on pure $Ti_3C_2T_x$ to fix single TM atoms.[72,73] Therefore, we established a pure $Ti_3C_2T_x$ with oxygen groups covering its surface ($Ti_3C_2O_2$). As introduced previously, the B atom can replace the position of the surface oxygen functional group and be used as the coordination atom to fix the TM atom when doped in $Ti_3C_2O_2$ ($Ti_3C_2O_{2-x}B_x$). As shown in Fig. 1a and b, two possible hollow sites (H1 and H2) might present to locate the TM on the surface of $Ti_3C_2O_2$

 

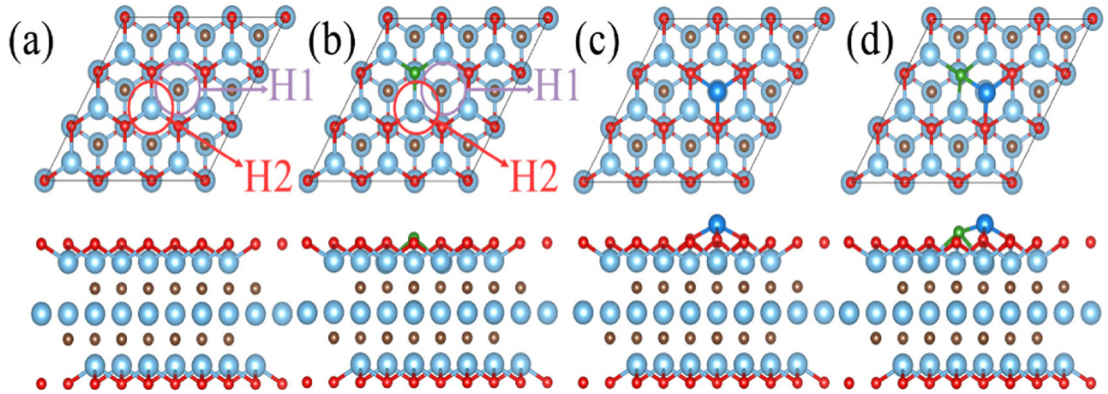


Fig. 1 Optimized models of (a) pure $Ti_3C_2O_2$ and (b) $Ti_3C_2O_{2-x}B_x$; color scheme: Ti, cyan; C, brown; O, red; B, green; and TM, blue. Circles represent the possible sites of TM on $Ti_3C_2O_2$. Optimized structures of (c) pure $Ti_3C_2O_2$ and (d) $Ti_3C_2O_{2-x}B_x$ monolayer confining TM single atoms at the H1 site.

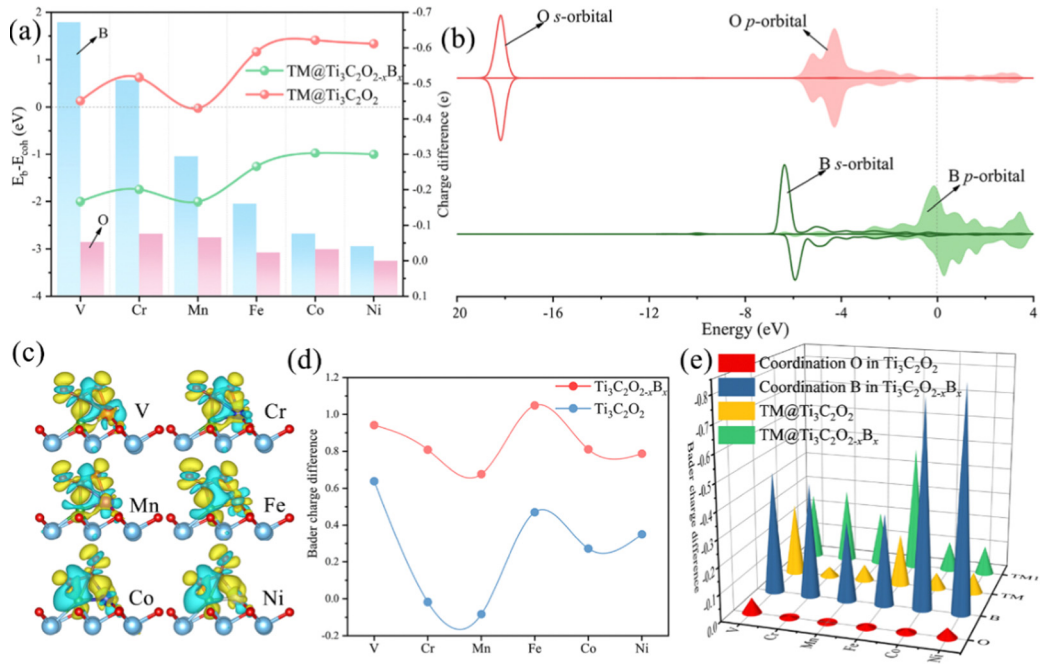


Fig. 2 (a) The $E_b$–$E_{coh}$ values of TM@$Ti_3C_2O_{2-x}B_x$ and TM@$Ti_3C_2T_x$ (line chart), charge differences of B and O atoms before and after anchoring a single TM atom (histogram). (b) PDOSs (projected density of states) of the O or B surface atoms before fixing the TM single atoms. (c) Variation of charge density differences of TM@$Ti_3C_2O_{2-x}B_x$ with a $CO_2$ adsorption configuration. The yellow region denotes charge accumulation and the blue region indicates charge depletion, where the isosurface value is set to be 0.03 e Å$^{-3}$. (d) Bader charge differences of the C atom in $CO_2$ before and after adsorption on TM@$Ti_3C_2O_{2-x}B_x$ and TM@$Ti_3C_2T_x$. (e) Bader charge differences of TM atoms, the coordination O atom in TM@$Ti_3C_2O_2$ and the coordination B atom in TM@$Ti_3C_2O_{2-x}B_x$ before and after $CO_2$ adsorption.

and $Ti_3C_2O_{2-x}B_x$. Previous studies, both theoretical and experimental, have identified that the H1 site is a stable adsorption site for metal atoms (Fig. 1c and d).[51,55]

Thermodynamically, the aggregation of the dispersed TM atoms depends on the bond strength between the TM and the substrate as well as the recombination ability of metal atoms. Therefore, the stability of SACs can be measured using the values of $E_b$–$E_{coh}$ of the TM and substrate (eqn (1) and (2)): the smaller this value the more thermodynamically stable the structure of SACs (Table S1, ESI†). For all of the TM atoms, the value of $E_b$–$E_{coh}$ for TM@$Ti_3C_2O_{2-x}B_x$ is lower than that for TM@$Ti_3C_2O_2$, suggesting that the presence of B is advantageous for stabilizing TM atoms (Fig. 2a). This can be explained by the fact that B atoms bind TM atoms through substantial partial charge transferred from the latter to the former. When the B atom is doped into the $Ti_3C_2O_2$ substrate, two electrons are transferred from the latter to the former, leaving the partial 2p orbital with lack of electrons. The empty 2p orbital helps the B atom gaining more electrons from the TM single atom than from O atom (Fig. 2a), leading to a thermodynamically more stable structure.

As shown in Fig. 2b, since the localized 2s orbital of the O atom is in the deep energy level, it is difficult for this orbital to

participate in bonding. The 2p orbital of the O atom is almost below the Fermi level, implying that it is fully occupied. The O atom with a saturated electronic structure is not conducive for receiving electrons from TM atoms. Compared with the O atom, the 2s orbital of the B atom is localized in a shallower energy level that is adjacent to its 2p orbital. The 2s orbital of the B atom and the d orbitals of the TM atom have obvious overlaps in the energy level ranging from −6 to 0 eV, indicating intense interactions between the TM and B atoms (Fig. S1, ESI†).

A part of the 2s orbital of the B atom is at the delocalization state and slightly contributes to the electronic state at the Fermi level, demonstrating the hybridization of B s–p orbitals. The partial 2p orbital of the B atom is above the Fermi level and the unoccupied 2p orbital can accept electrons from TM atoms to form strong-polarized covalent TM–B bonds. In addition, we have calculated the area of the H1 site, which is defined as the triangular area enclosed by three oxygen atoms in $Ti_3C_2O_2$ or two oxygen atoms and one boron atom in $Ti_3C_2O_{2-x}B_x$ (Fig. S2, ESI†). The calculated area of the H1 site of $Ti_3C_2O_{2-x}B_x$ (4.21 Å$^2$) is larger than that of $Ti_3C_2O_2$ (4.11 Å$^2$). The larger area in the former provides more spacious H1 sites so that TM atoms can be effectively embedded into the flat substrate of $Ti_3C_2O_{2-x}B_x$. Since our results suggest that $Ti_3C_2O_{2-x}B_x$ has an outstanding ability to fix TM single atoms, all the six kinds of metal are considered in the following $CO_2$RR investigation.

### 3.2. $CO_2$ electroreduction reaction on TM@$Ti_3C_2O_{2-x}B_x$ SACs

**3.2.1. Initial activation of $CO_2$.** One method of effective activation of $CO_2$ is changing its linear structure (O═C═O) to a V-shaped ($\angle OCO < 180^\circ$) structure, where partially negatively charged $CO_2$ is generated due to the injection of electrons into its antibonding $2\pi_u^*$ orbital. As shown in Fig. S3 (ESI†), $CO_2$ binds to TM@$Ti_3C_2O_{2-x}B_x$ (TM is V, Cr, Mn or Fe) through a B–C–TM–O configuration, but to TM@$Ti_3C_2O_{2-x}B_x$ (TM is Co or Ni) through an O–B–C–TM configuration. The linear O═C═O is bent substantially and its C atom binds to the TM atom and the nearby B atom in both configurations. These bonding configurations indicate that the B atom can participate in the $CO_2$ adsorption. In the case of TM@$Ti_3C_2O_2$ (Fig. S3, ESI†), $CO_2$ binds to TM (TM is V, Fe, Co or Ni) through a bidentate C–TM–O configuration with a bent structure, but binds to TM (TM is Cr or Mn) through a monodentate O–M configuration with a linear structure. This reveals that TM@$Ti_3C_2O_2$ (TM is V, Fe, Co or Ni) also has the ability to activate $CO_2$ molecules. However, for all the TM@$Ti_3C_2O_2$ considered, $CO_2$ molecules only bind to the TM atom, implying that the O atom of the functional groups does not participate in the $CO_2$ activation directly. As can be seen in Table 1, the bending angle of the $CO_2$ adsorbed on TM@$Ti_3C_2O_{2-x}B_x$ is smaller than that on TM@$Ti_3C_2O_2$, suggesting a more significant $CO_2$ activation in the former.

Table 1 Binding energy (BE), binding distance (BD), and bond angle (BA) of $CO_2$ adsorbed on TM@$Ti_3C_2O_{2-x}B_x$ and TM@$Ti_3C_2O_2$ in the most stable configuration

| | $Ti_3C_2O_{2-x}B_x$ | | | | $Ti_3C_2O_2$ | | |
|---|---|---|---|---|---|---|---|
| | BE | BD (Å) | | BA | BE | BD (Å) | BA |
| Metal | (eV) | TM–C | B–C | ($\angle$OCO, °) | (eV) | TM–C | ($\angle$OCO, °) |
| V | −1.49 | 2.12 | 1.72 | 128.7 | −0.62 | 2.01 | 140.7 |
| Cr | −1.03 | 2.10 | 1.74 | 130.5 | −0.65 | — | 179.7 |
| Mn | −0.52 | 2.15 | 1.81 | 136.5 | −0.48 | — | 179.4 |
| Fe | −0.73 | 2.48 | 1.62 | 126.5 | −0.27 | 2.06 | 151.9 |
| Co | −1.34 | 1.86 | 1.82 | 125.3 | −0.09 | 2.09 | 158.9 |
| Ni | −1.62 | 1.89 | 1.82 | 126.8 | −0.25 | 1.98 | 153.5 |

These phenomena we discussed above indicate that the doping of B facilitates the activation of $CO_2$ through participating in its adsorption process. To understand the emerging role of the B atom in $CO_2$ activation, we examine the electronic structures of TM@$Ti_3C_2O_{2-x}B_x$ and TM@$Ti_3C_2O_2$ through a Bader charge analysis. The images of the charge density difference of the $CO_2$ adsorbed TM@$Ti_3C_2O_{2-x}B_x$ are shown in Fig. 2c. As seen, charge accumulated in the $CO_2$ $2\pi_u^*$ antibonding orbital around the C atom, leading to the activation of $CO_2$ molecules. In contrast, charge depleted around B and TM atoms, confirming that the electrons involved in the activation of $CO_2$ come from these atoms. To give more details of charge transfer density, Bader effective charge is investigated. When adsorbed on the surface, the C atom of $CO_2$ in the case of TM@$Ti_3C_2O_{2-x}B_x$ can gain more electrons than that in the case of TM@$Ti_3C_2O_2$ (Fig. 2d).

Generally, the strong electronegativity of oxygen shifts the focus of electronic clouds on both ends of $CO_2$ molecules, yielding an electron-deficient carbon center. An injection of electron into the C atom is an effective way to activate $CO_2$ molecules. The observation that TM@$Ti_3C_2O_{2-x}B_x$ has a more activated $CO_2$ is consistent with the results of calculations. Bader effective charge analysis (Fig. 2e) also shows that B and TM atoms can provide enough electrons for injection into $CO_2$ molecules. In particular, in the cases of Co@$Ti_3C_2O_{2-x}B_x$ and Ni@$Ti_3C_2O_{2-x}B_x$, most of the injected electrons come from the B atom. When $CO_2$ molecules are activated on TM@$Ti_3C_2O_2$, the $Ti_3C_2O_2$ substrate can provide extra electrons to activate $CO_2$, which is consistent with our previous result.[56] But an indirect participation mode provides less electron than a direct participation.

The reaction activity of the doped B atom can be ascribed to its occupied 2p orbitals with s–p hybridization. Because the electronegativity of B is weaker than that of C, the electrons in the occupied orbitals of the B atom can transfer easily to the C atom of the $CO_2$ molecule. In contrast, the full 2p-orbital occupation electronic structure of the O atom leads to a strong chemical stability. The stronger electronegativity of the O atom also makes it difficult for the C atom to grab its electrons. To gain insights into the chemisorption of $CO_2$ on the active site of TM@$Ti_3C_2O_{2-x}B_x$, the bonding states of $CO_2$ on TM@$Ti_3C_2O_{2-x}B_x$ were investigated. According to the projected density of states (PDOS) for an isolated $CO_2$ molecule (Fig. 3a–d and Fig. S4, ESI†), the empty orbital above the Fermi level is the antibonding $2\pi_u^*$ orbital.

According to the PDOS of bare TM@$Ti_3C_2O_{2-x}B_x$, TM 3d overlaps with B 2p, indicating the bonding of TM and B atoms.

 

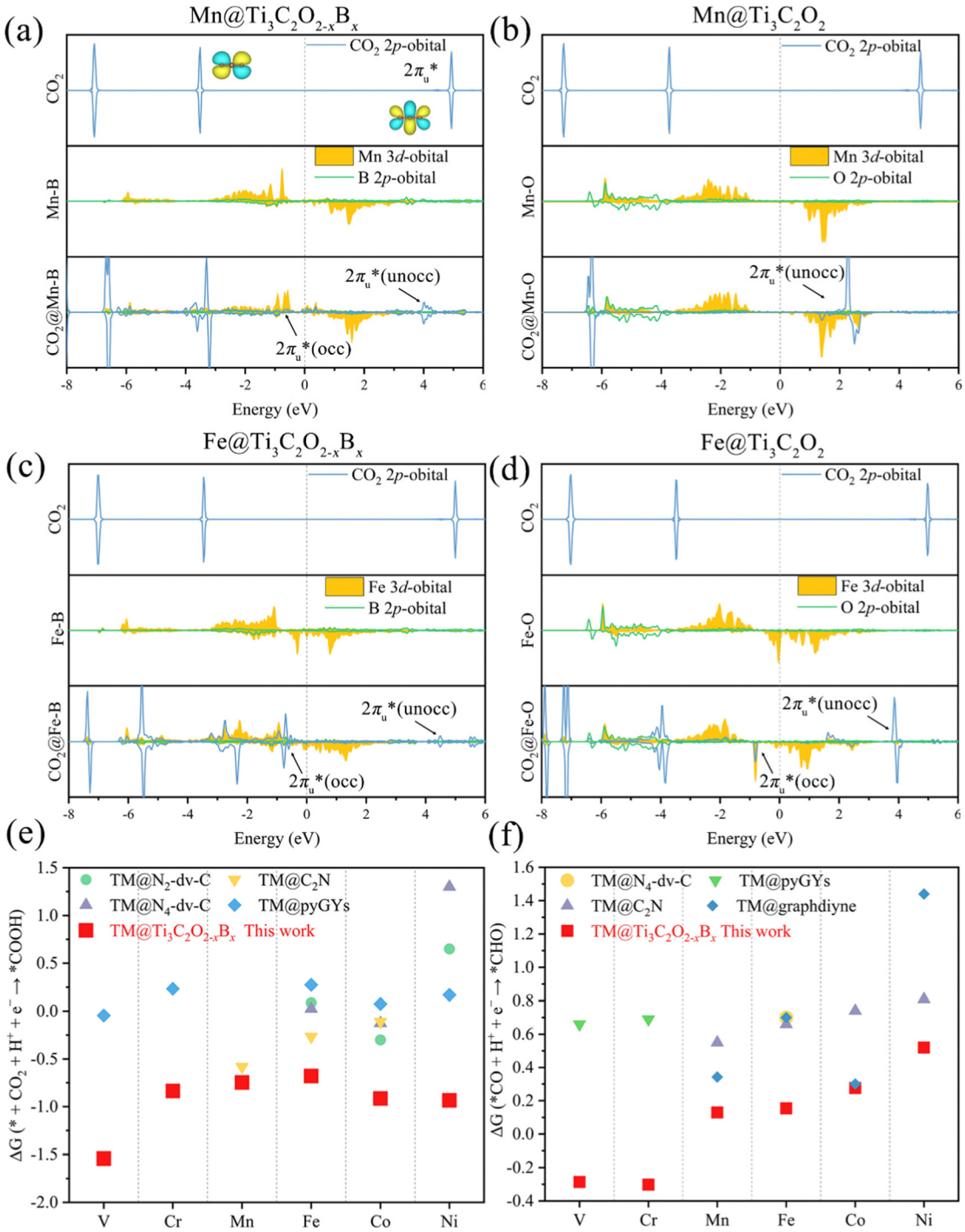


Fig. 3 The PDOS of $CO_2$ 2p, TM 3d, and coordination atoms (the O atom in $TM@Ti_3C_2O_2$ and the B atom in $TM@Ti_3C_2O_{2-x}B_x$) of the 2p orbital before and after $CO_2$ adsorption on (a) $Mn@Ti_3C_2O_{2-x}B_x$, (b) $Mn@Ti_3C_2O_2$, (c) $Fe@Ti_3C_2O_{2-x}B_x$ and (d) $Fe@Ti_3C_2O_2$. A comparison of the Gibbs free energy changes of (e) the 1st ($CO_2 + H^+ + e^- \rightarrow$ *COOH) and (f) the 3rd ($CO + H^+ + e^- \rightarrow$ *CHO) hydrogenation reactions for $TM@Ti_3C_2O_{2-x}B_x$ and other SACs ($TM@N_2$-dv-C,[74] $TM@N_4$-dv-C,[74] $TM@C_2N$,[75] TM@pyGYs,[76] and TM@graphdiyne[77]) for the $CO_2$ reduction.

After its adsorption on $TM@Ti_3C_2O_{2-x}B_x$, the antibonding $2\pi_u^*$ of $CO_2$ splits into two parts: one above and one below the Fermi level. The states above the Fermi level are contributed by the unoccupied TM 3d-$CO_2$ $2\pi_u^*$ and B 2p-$CO_2$ $2\pi_u^*$ hybridization orbitals, while the overlapping of occupied TM 3d-$CO_2$ $2\pi_u^*$ and B 2p-$CO_2$ $2\pi_u^*$ hybridization orbitals can be found at −2 to 0 eV, just below the Fermi level. After adsorbing on $TM@Ti_3C_2O_2$, the antibonding $2\pi_u^*$ orbital of $CO_2$ also splits into one part above the Fermi level and one part below it. Notably, the peak intensity of the unoccupied $CO_2$ $2\pi_u^*$ orbital when $CO_2$ adsorbed on $TM@Ti_3C_2O_{2-x}B_x$ decreases more sharply than that when $CO_2$ adsorbed on $TM@Ti_3C_2O_2$. This implies that

$TM@Ti_3C_2O_{2-x}B_x$ provides more electrons that can be injected into the $2\pi_u^*$ orbital, which is consistent with the results of Bader charge analysis.

Besides $CO_2$ activation ability, another key issue in $CO_2$RR catalyst design is to obtain an energy-rich product ($CH_4$), which is closely related to the adsorption Gibbs free energy of radical reaction intermediates and that of the elementary $CO_2$ reduction reaction. $CO_2$RR can be differentiated by the types of intermediates formed in the initial protonation steps of $CO_2$: formate (*OCHO) and carboxyl (*COOH). The calculated Gibbs free energy changes ($\Delta G$) for the formation of *COOH and *OCHO ($*CO_2 + H^+ + e^- \rightarrow$ *COOH or *OCHO) on $TM@Ti_3C_2O_{2-x}B_x$ are summarized in Fig. S5 (ESI†). This figure shows that the 1st hydrogenation ($H^+/e^-$) reactions are energetically prone to occur on the O atom rather than on the C atom, suggesting that the formation of *COOH is more energetically preferred than that of *OCHO. The calculated $\Delta G$ shown in Fig. 3e reveals that the $\Delta G$ of the first hydrogenation reaction to form *COOH on $TM@Ti_3C_2O_{2-x}B_x$ is smaller than that in previous studies, illustrating the superior $CO_2$ activation ability of $TM@Ti_3C_2O_{2-x}B_x$.

**3.2.2. Origin of CO activity on $TM@Ti_3C_2O_{2-x}B_x$.** According to previous studies, *COOH will always lead to the formation of *CO *via* releasing one $H_2O$ molecule, and further reduce to intermediate *CHO.[14,74,75] Besides *COOH, *CO is another crucial intermediate in the $CO_2$RR to form $CH_4$, the adsorption energy of which is closely related to $CO_2$RR performance. The weak CO adsorption on SACs results in direct desorption of CO under low electrode potentials. Therefore, a stably adsorbed CO on SACs may improve its further reduction towards $CH_4$.

The relatively higher CO adsorption strength on $TM@Ti_3C_2O_{2-x}B_x$ (Table S2, ESI†) results in poor activity for CO direct desorption under low electrode potentials. Due to the outstanding stability of CO, the hydrogenation reaction needs too much energy to reduce *CO. If the $\Delta G$ of the reaction $*CO + H^+ + e^- \rightarrow$ *CHO is larger than that of the reaction $*CO \rightarrow CO + *$, CO is inclined to desorb rather than further hydrogenation. However, a high voltage is still needed to remove *CO from the surface if the adsorption of CO on the catalyst is strong. In general, the lower hydrogenation $\Delta G$ of the reaction $*CO + H^+ + e^- \rightarrow$ *CHO is necessary for the further CO reduction process. Therefore, the activation of the *CO intermediate is a key criterion to evaluate the performance of the $CO_2$RR on SACs.

To verify the performance of $TM@Ti_3C_2O_{2-x}B_x$ in *CO reduction, we calculated the $\Delta G$ of the reaction $*CO + H^+ + e^- \rightarrow$ *CHO, along with the $\Delta G$ of other SACs. Having examined the available results for the $CO_2$RR of SACs, we can find that $*CO + H^+ + e^- \rightarrow$ *CHO is the potential-determining step in most of these studies. As shown in Fig. 3f, the calculated $\Delta G$ for the reaction $*CO + H^+ + e^- \rightarrow$ *CHO on $TM@Ti_3C_2O_{2-x}B_x$ is smaller than the corresponding values of $\Delta G$ reported in previous studies, which verifies the superior CO activation ability of $TM@Ti_3C_2O_{2-x}B_x$. According to the adsorption configuration of *CO on $TM@Ti_3C_2O_{2-x}B_x$, the B atom also participates in the adsorption process (Fig. 4a), demonstrating its important role in CO activation. To gain insights into the combined effect of multi-active site TM and B atoms in ameliorating the CO reduction, the orbital and charge transfer of TM and B atoms during the adsorption of *CO is also investigated. The configuration of the *CO adsorbed on $TM@Ti_3C_2O_2$ is used for comparison.

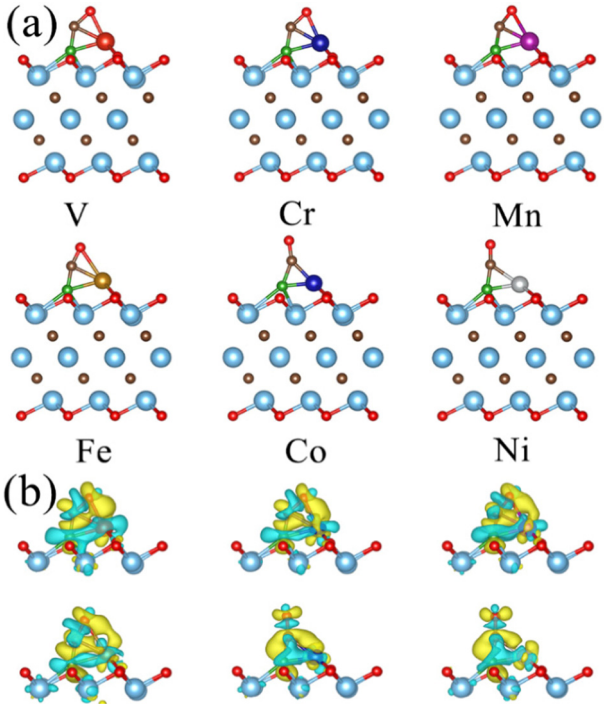


Fig. 4 (a) Optimized geometric structures of CO adsorbed on $TM@Ti_3C_2O_{2-x}B_x$. (b) Variation in the difference of charge density of $TM@Ti_3C_2O_{2-x}B_x$ with a CO adsorption configuration. The yellow region denotes charge accumulation and the blue region indicates charge depletion, where the isosurface value is set to be 0.03 e $Å^{-3}$.

Accepting the lone-pair electrons from the $\sigma_g$ orbital of CO and donating electrons to the antibonding $\pi_g^*$ orbitals of CO are the main ways to weaken the C≡O triple bond, known as the "acceptance–donation" process.[78,79] Fig. 4b and Fig. S6 (ESI†) illustrate the calculated charge density differences for the CO adsorption configuration on $TM@Ti_3C_2O_{2-x}B_x$ and $TM@Ti_3C_2O_2$. Charge accumulation and depletion can be observed for both CO molecules and B–TM atoms on $TM@Ti_3C_2O_{2-x}B_x$. This phenomenon is actually in perfect accordance with the "acceptance–donation" process mentioned above. A comparison between the area of the isosurface of CO adsorbed on $TM@Ti_3C_2O_{2-x}B_x$ and that on $TM@Ti_3C_2O_2$ reveals that the charge transfer in the former is more obvious than that in the latter.

To further elucidate the bonding nature, the PDOS of the adsorption of CO on $TM@Ti_3C_2O_{2-x}B_x$ and that on $TM@Ti_3C_2O_2$ are investigated (Fig. 5 and Fig. S7, ESI†). After adsorbing on $TM@Ti_3C_2O_{2-x}B_x$ and $TM@Ti_3C_2O_2$, the $\sigma_g$ orbital of CO in a deep level obviously splits and moves to deeper energy states, indicating the interaction between the CO $\sigma_g$ orbital and SACs. It can be seen that a part of the $\pi_g^*$ orbitals of CO unoccupied (unocc) shifts upward to the Fermi level and the

 

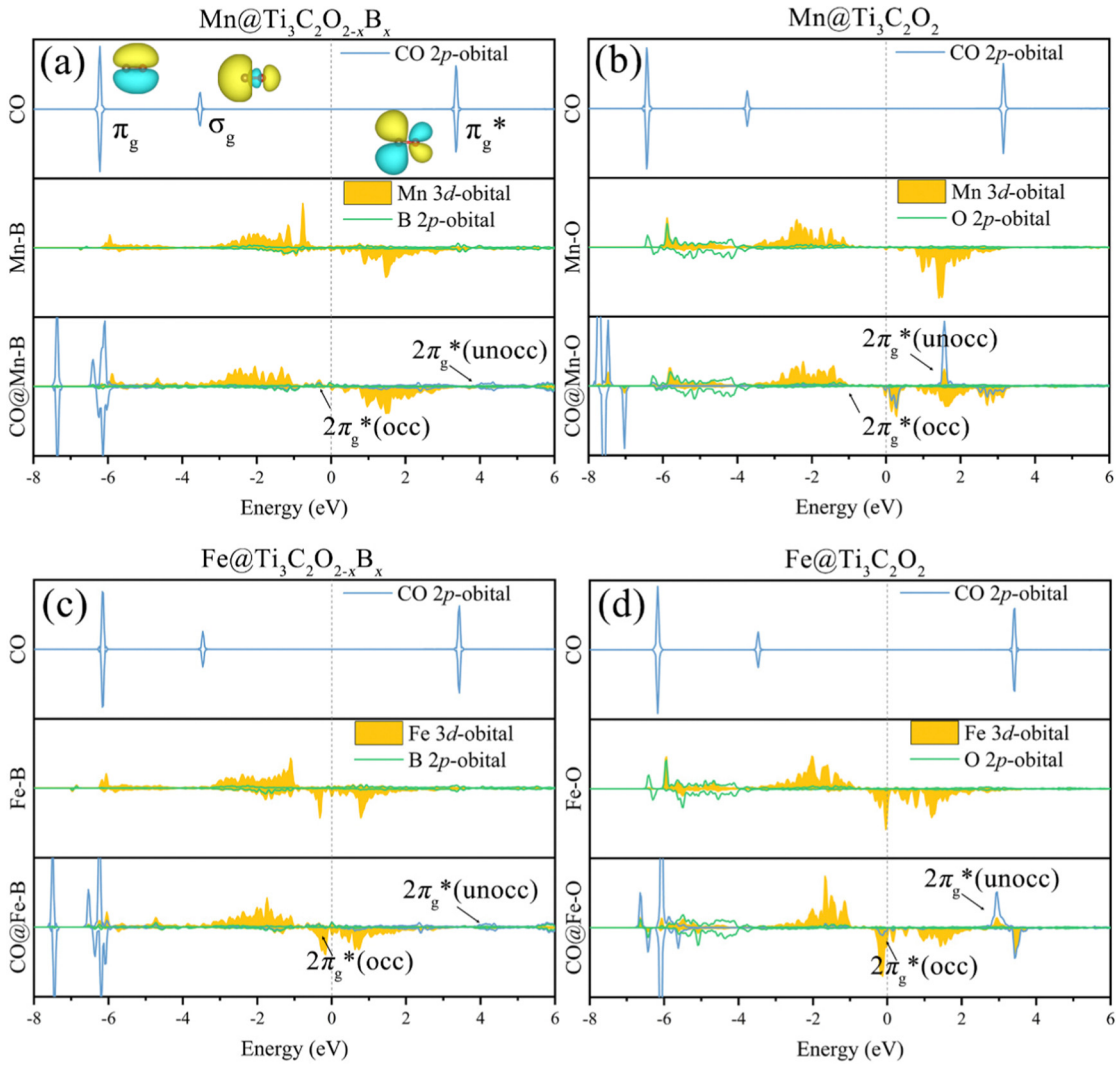


Fig. 5 The PDOS of CO 2p, TM 3d, and coordination atoms (the O atom in TM@$Ti_3C_2O_2$ and the B atom in TM@$Ti_3C_2O_{2-x}B_x$) of the 2p orbital before and after $CO_2$ adsorption on (a) Mn@$Ti_3C_2O_{2-x}B_x$, (b) Mn@$Ti_3C_2O_2$, (c) Fe@$Ti_3C_2O_{2-x}B_x$ and (d) Fe@$Ti_3C_2O_2$.

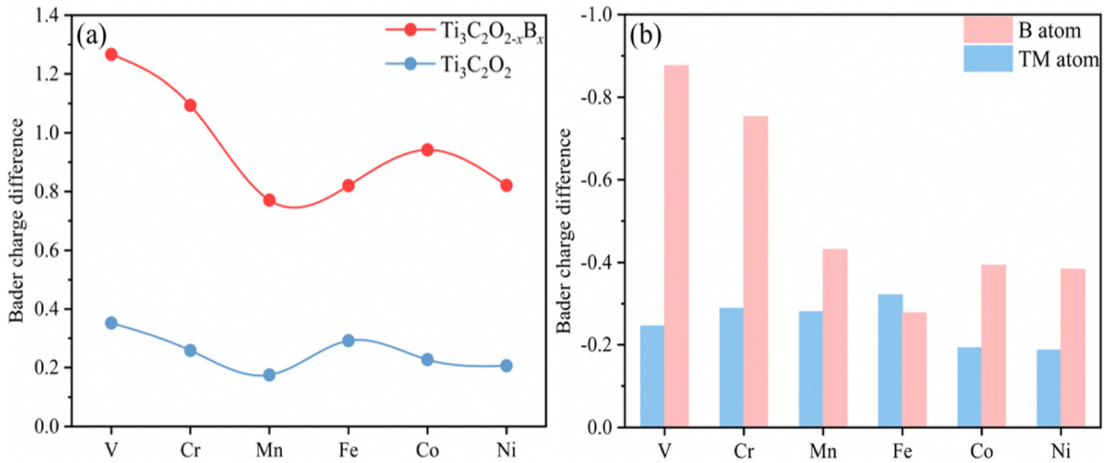


Fig. 6 (a) Bader charge differences of the C atom in CO before and after adsorption on TM@$Ti_3C_2O_{2-x}B_x$ and TM@$Ti_3C_2T_x$. (b) Bader charge differences of TM atoms and the B atom on TM@$Ti_3C_2O_{2-x}B_x$ before and after CO adsorption.

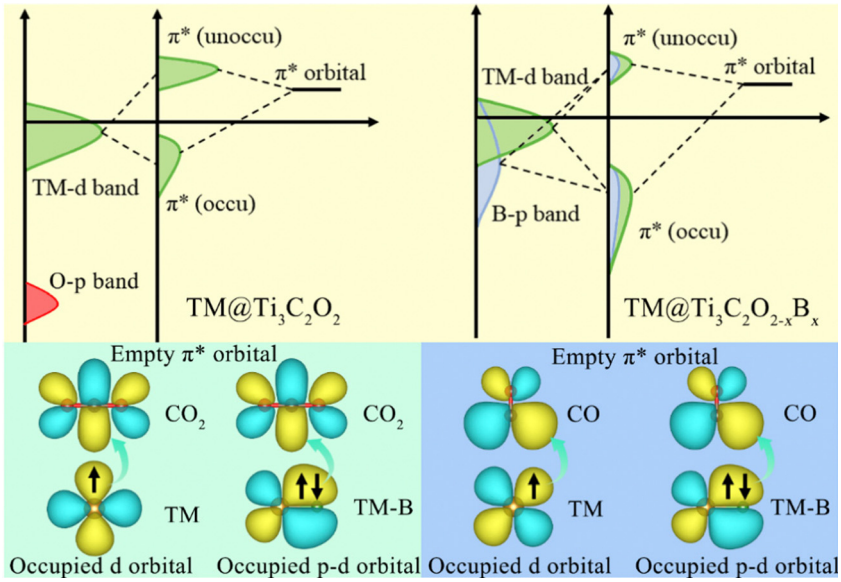


Fig. 7 Schematic diagrams of $CO_2$ molecule and CO intermediate activation mechanisms on $TM@Ti_3C_2O_2$ and $TM@Ti_3C_2O_{2-x}B_x$.

other part moves downward to the Fermi level near −2 eV to form a $\pi_g^*$ occupied (occ) orbital. Compared with that of $TM@Ti_3C_2O_2$, the peak intensity of the unoccupied CO $\pi_g^*$ antibonding orbital decreases more sharply when CO is adsorbed on $TM@Ti_3C_2O_{2-x}B_x$, indicating the better CO activation performance of $TM@Ti_3C_2O_{2-x}B_x$. The Bader charge analysis shows that the C atom from CO can gain more electrons from $TM@Ti_3C_2O_{2-x}B_x$ (Fig. 6a and b), which is consistent with the above PDOS analysis.

Owing to its weak electronegativity and not fully occupied orbital structure, the electrons in the occupied orbitals of the B atom can easily transfer to the empty orbitals of the $CO_2$ molecule and CO intermediate. Based on the results gathered, it can be reasonably inferred that a combined effect between the single TM atom and B atom is present on the $CO_2$RR (Fig. 7). The TM-to-C and B-to-C π-back bonding contribute to the activation of the $CO_2$ molecules and CO intermediate. Enough electrons from the single TM atom and B atom can be injected into $CO_2$ and CO molecules through a direct bonding interaction. Therefore, the B-doping strategy efficiently controls the charge–orbital state of the coordination atom on the surface of $Ti_3C_2T_x$-MXene, alleviating remarkably the difficulty of activating $CO_2$ and CO molecules.

**3.2.3. Subsequent protonation steps toward $CO_2$RR production.** The excellent activation performance endows $TM@Ti_3C_2O_{2-x}B_x$ SACs with great potential for the $CO_2$RR. The outstanding CO activation performance can also help its further reduction reaction towards methane on $TM@Ti_3C_2O_{2-x}B_x$ SACs. Using the electronic potential energy surface (PES) as a baseline, we examine the subsequent protonation steps *via* the *COOH intermediate to form final product $CH_4$(g) in this section.

Fig. 8 shows the variation of the calculated free energy with the most favorable pathway for the reduction of $CO_2$ on $TM@Ti_3C_2O_{2-x}B_x$ SACs and the corresponding structures of the reaction intermediates are presented in Fig. S8 (ESI†). Owing to the excellent $CO_2$ activation performance of $TM@Ti_3C_2O_{2-x}B_x$, the hydrogenation of the adsorbed $CO_2$ to form *COOH is exothermic with a negative $\Delta G$. The 3rd hydrogenation ($H^+/e^-$) reaction of *CO occurs, generating *CHO. *CO is more likely to undergo further reduction on all the $TM@Ti_3C_2O_{2-x}B_x$ because the $\Delta G$ of the protonation step ($*CO + H^+ + e^- \rightarrow *CHO$) is more negative than that of CO desorption. Therefore, we concluded that the production of CO can be effectively prohibited in the $CO_2$ reduction. The small $\Delta G$ of the 3rd hydrogenation also implies that the adsorbed *CO, which is generally regarded as the poison on metallic electrodes, is less likely to poison the active sites in our case.

For the subsequent elementary reaction steps passing through the CHO* intermediate to generate $CH_4$, it is worth mentioning that the desorption of $CH_2O$ from $TM@Ti_3C_2O_{2-x}B_x$ is significantly endothermic due to their large negative adsorption energies (Table S2, ESI†), indicating that the production of methanol ($CH_2O$) can be effectively prevented during the reduction of $CO_2$ catalyzed by $TM@Ti_3C_2O_{2-x}B_x$. In addition, $*CH_3O$ is more likely to be further reduced to *O, releasing one $CH_4$ molecule on $TM@Ti_3C_2O_{2-x}B_x$ (TM is V, Cr or Mn). Therefore, the production of $CH_3OH$ can be avoided effectively. For the case of $TM@Ti_3C_2O_{2-x}B_x$ (TM is Fe, Co or Ni), the desorption $\Delta G$ of $CH_3OH$ is appreciably large so that the desorption of $CH_3OH$ is difficult. After $*CH_3OH$ is formed on $TM@Ti_3C_2O_{2-x}B_x$, its C atom will be attacked by a proton to form $CH_4$(g) and *OH. This suggests that $CH_4$ is the primary reduction product on all the $TM@Ti_3C_2O_{2-x}B_x$ examined, indicating its great selectivity for catalyzing the $CO_2$ reduction to form $CH_4$ with excellent abilities to limit the production of CO(g), $CH_2O$(g), and $CH_3OH$(l).

 

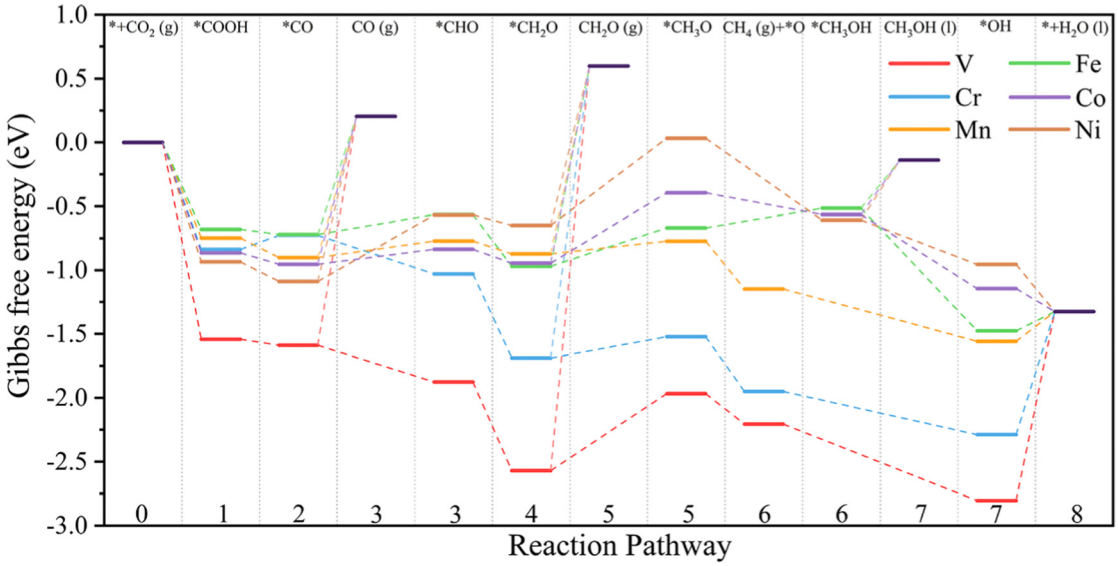


Fig. 8 Variation of the Gibbs free energy for the reduction reaction of $CO_2$ on TM@$Ti_3C_2O_{2-x}B_x$ (TM is V, Cr, Mn, Fe, Co or Ni,) at 0 V with RHE.

To assess the durability of TM@$Ti_3C_2O_{2-x}B_x$ SACs in practical application, we have further investigated the protonation of remaining *OH as well as the release of the adsorbed $H_2O$ molecule (8th hydrogenation reaction). The results obtained show that the *OH on TM@$Ti_3C_2O_{2-x}B_x$ (TM is V or Cr) is harder to be removed; the uphill values of $\Delta G$ are 1.47 and 0.96 eV, respectively. The positive $\Delta G$ indicates that *OH is more likely to occupy active sites by forming TM–OH, which hinders the next $CO_2$ reduction process. For other TM@$Ti_3C_2O_{2-x}B_x$ (TM is Mn, Fe, Co or Ni), the formation of *CHO ($*CO + H^+ + e^- = *CHO$) and *$CH_3O$ ($*CH_2O + H^+ + e^- = *CH_3O$) is both endothermic and the rest of the elementary steps are exothermic.

Except Mn@$Ti_3C_2O_{2-x}B_x$, the uphill value of $\Delta G$ for the formation of *$CH_3O$ on TM@$Ti_3C_2O_{2-x}B_x$ (TM is Fe, Co or Ni) is larger than that for the formation of *CHO. Therefore, the formation of *CHO and *$CH_3O$ is the potential-determining step (PDS) for Mn@$Ti_3C_2O_{2-x}B_x$ and TM@$Ti_3C_2O_{2-x}B_x$ (TM is Fe, Co or Ni), respectively. The PDS and the values of $U_L$ predicted by DFT are summarized in Table 2. Based on the $U_L$ calculated from the primary PDS, it can be inferred that Mn@$Ti_3C_2O_{2-x}B$ and Fe@$Ti_3C_2O_{2-x}B$ have a higher activity for $CH_4$ production, where their limiting potentials are 0.13 and 0.3 V, respectively, lower than those of other TM@$Ti_3C_2O_{2-x}B_x$.

Table 2 DFT-predicted potential determining steps (PDSs), $U_L$ values, and possible products on TM@$Ti_3C_2O_{2-x}B_x$

| Catalyst | Potential determining step | $U_L$ (V) | Production |
|---|---|---|---|
| V@$Ti_3C_2O_{2-x}B_x$ | $*OH + H^+ + e^- \rightarrow H_2O$ (l) | 1.47 | $CH_4$ |
| Cr@$Ti_3C_2O_{2-x}B_x$ | $*OH + H^+ + e^- \rightarrow H_2O$ (l) | 0.96 | $CH_4$ |
| Mn@$Ti_3C_2O_{2-x}B_x$ | $*CO + H^+ + e^- \rightarrow *CHO$ | 0.13 | $CH_4$ |
| Fe@$Ti_3C_2O_{2-x}B_x$ | $*CH_2O + H^+ + e^- \rightarrow *CH_3O$ | 0.30 | $CH_4$ |
| Co@$Ti_3C_2O_{2-x}B_x$ | $*CH_2O + H^+ + e^- \rightarrow *CH_3O$ | 0.55 | $CH_4$ |
| Ni@$Ti_3C_2O_{2-x}B_x$ | $*CH_2O + H^+ + e^- \rightarrow *CH_3O$ | 0.68 | $CH_4$ |

We conclude that Mn@$Ti_3C_2O_{2-x}B_x$ and Fe@$Ti_3C_2O_{2-x}B_x$ have a remarkable selectivity and activity for the production of $CH_4$(g). Considering the effect of the presence of water under real reaction conditions, we calculated the free energy diagram of the initial screening for Mn@$Ti_3C_2O_{2-x}B$ and Fe@$Ti_3C_2O_{2-x}B$ in the implicit solvent model using VASPsol (Fig. 9a and b). Notably, the levels of $U_L$ for Mn@$Ti_3C_2O_{2-x}B$ and Fe@$Ti_3C_2O_{2-x}B$ increased to 0.51 and 0.40 V, respectively. The overpotential of Fe@$Ti_3C_2O_{2-x}B$ (0.40 V) suggests that it can be a promising $CO_2$RR catalyst for producing $CH_4$. This level of limiting potentials is comparable or lower than those of the widely employed transition metal-based $CO_2$RR electrocatalysts[8,14,80] and other bimetallic electrocatalysts work on $CO_2$ conversion to $CH_4$ (Table S3, ESI†).

### 3.3. Stability of Fe@$Ti_3C_2O_{2-x}B_x$ in solution and competition between the $CO_2$RR and the HER

Apart from $CO_2$ adsorption, the competitive adsorption of $CO_2$RR and H on each active center is also a significant factor affecting $CO_2$RR performance. The free energy of hydrogen adsorption ($\Delta G_H$) provides a measure for evaluating HER activity. A material is an optimal HER electrocatalyst if its $\Delta G_H$ value is close to zero. However, a highly negative $\Delta G_H$ indicates the excessively stable adsorption of H on the active sites, thereby preventing the $CO_2$RR. Therefore, active sites with a large $\Delta G_H$ are desirable for $CO_2$RR electrocatalysts. Assuming a Volmer and Tafel mechanism, we calculated the $\Delta G$ for the formation of *COOH ($* + CO_2 + H^+ + e^- \rightarrow *COOH$) and that for the formation of *H ($H^+ + e^- \rightarrow *H$) in the HER. According to Brønsted–Evans–Polanyi (BEP) relations, a reaction with a more negative $\Delta G$ is expected to encounter a smaller reaction barrier and, therefore, is more favored to occur.

The adsorption sites for the H atom mainly locate on the bridge site between the TM and B atoms on Fe@$Ti_3C_2O_{2-x}B_x$ (Fig. 9c). The calculated $\Delta G_H$ of Fe@$Ti_3C_2O_{2-x}B_x$ is −0.48 eV,

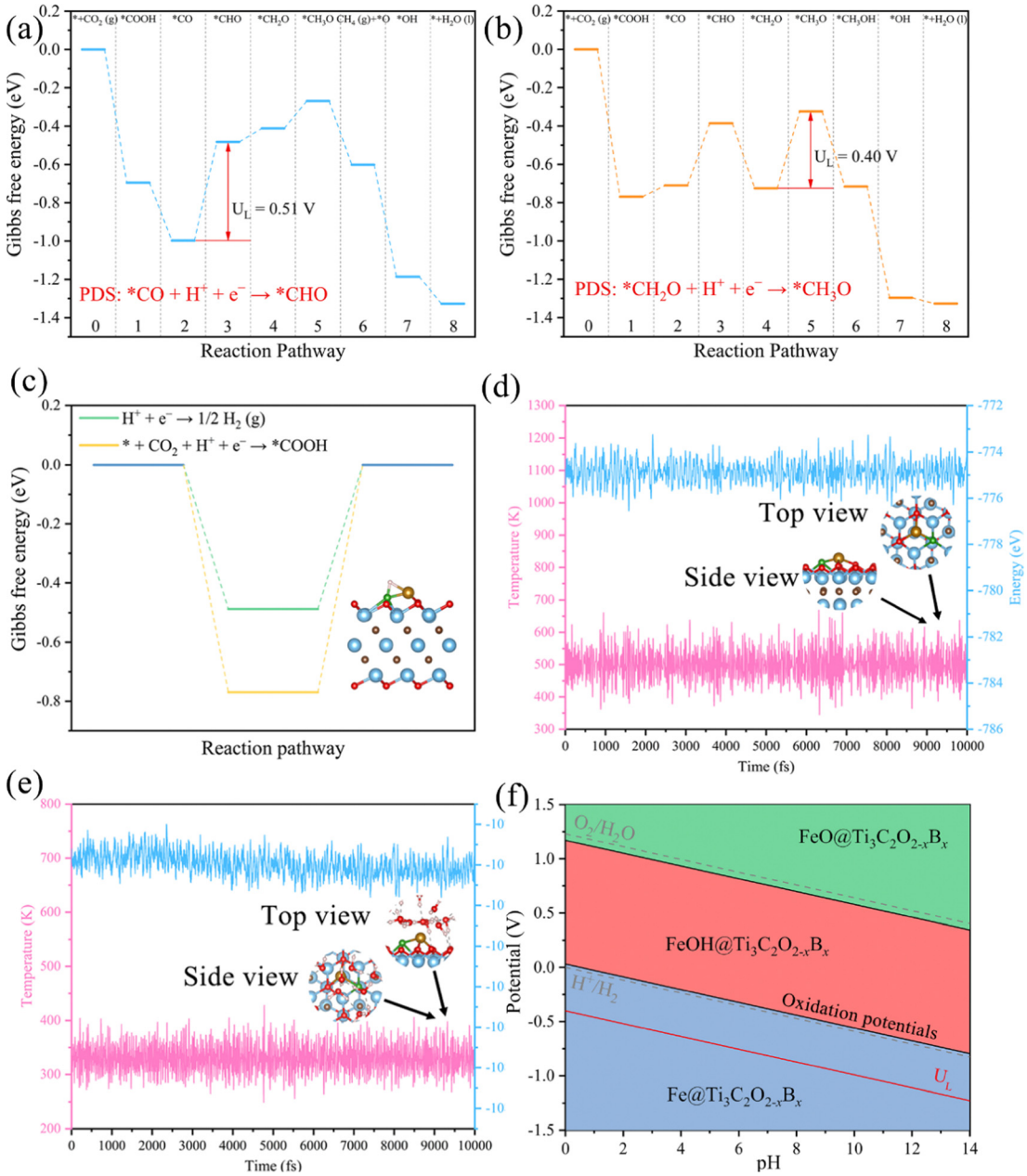


Fig. 9 Free energy diagrams of the $CO_2RR$ on (a) $Mn@Ti_3C_2O_{2-x}B$ and (b) $Fe@Ti_3C_2O_{2-x}B$ after taking into account of solvation effects. (c) Variation of the Gibbs free energy changes ($\Delta G$) for the first protonation step of the $CO_2RR$ with HER. Inset: the optimized geometric structures of H adsorbed on $Fe@Ti_3C_2O_{2-x}B_x$. (d) Variations of energy and temperature with the AIMD simulation time for $Fe@Ti_3C_2O_{2-x}B$, where the AIMD simulation lasts for 10 ps at 500 K. (e) Variations of energy and temperature with the AIMD simulation time for $Fe@Ti_3C_2O_{2-x}B$, an explicit solvent model is used to simulate the acidic aqueous solution. The AIMD simulation lasts for 10 ps at 330 K. (f) Calculated Pourbaix diagram of $Fe@Ti_3C_2O_{2-x}B$. Gray dashed lines denote the water redox potentials.

which is more positive than the $\Delta G_{*COOH}$ of the $CO_2RR$ (Fig. 9c). This suggests that $Fe@Ti_3C_2O_{2-x}B_x$ contains inactive sites for the HER with a $|\Delta G_H|$ of around 0.5 eV and exhibits a higher selectivity toward the $CO_2RR$ than the HER.

To assess the durability of MXene catalysts in practical applications, we investigated the stability of $Fe@Ti_3C_2O_{2-x}B_x$ *via* AIMD simulations. As seen in Fig. 9d, both the total energy and the temperature oscillate near the initial conditions and the geometric structures of $Fe@Ti_3C_2O_{2-x}B_x$ are preserved well within 10 ps. An explicit solvent model is also applied to simulate the solution environment, and AIMD simulations are performed to study the thermal stability of $Fe@Ti_3C_2O_{2-x}B_x$ in a solution at 330 K for 10 ns.

The results obtained reveal that the structure of $Fe@Ti_3C_2O_{2-x}B_x$ can remain stable in an aqueous solution (Fig. 9e). Therefore, it can be inferred that $Fe@Ti_3C_2O_{2-x}B_x$ can serve as an efficient $CO_2RR$ electrocatalyst under ambient conditions with a high stability. Further analysis of the Pourbaix diagram

 

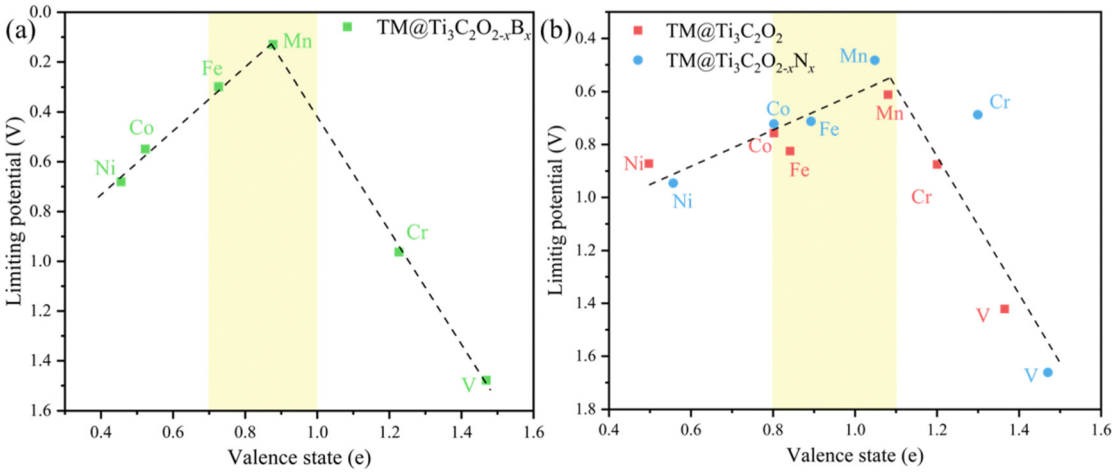


Fig. 10 The limiting potential as a function of the valence state of TM atoms fixed on (a) $Ti_3C_2O_{2-x}B_x$ and (b) $Ti_3C_2O_2$, $Ti_3C_2O_{2-x}N_x$.

of $Fe@Ti_3C_2O_{2-x}B_x$ (Fig. 9f) has also been carried out. It is a useful tool to identify the stable state of catalysts in water as a function of pH and applied potential. The oxidation potential of $Fe@Ti_3C_2O_{2-x}B_x$ at pH 0 (black line) is less negative than the $U_L$ value of $Fe@Ti_3C_2O_{2-x}B_x$ (red line), indicating that $Fe@Ti_3C_2O_{2-x}B_x$ could possess superior electrochemical stability against surface oxidation under working conditions.

### 3.4. An activity descriptor for $CO_2$ reduction on $Ti_3C_2T_x$-based SACs

It is beneficial to search an activity descriptor to establish a "volcano" relationship on catalytic behaviors so that we can further roughly estimate the effect of other potential dopants on the $CO_2$RR performance. It is generally agreed that the electronic structures of catalytic centers would greatly influence the electron transfer and reaction energy in catalytic processes. Pan and coworkers have found that the valence state of TMs could be used as an activity descriptor, wherefore the limiting potential towards different products as a function of the valence state of TMs[81] because the TM atoms can provide both empty d orbitals to accept electrons to form a coordination bond and lone electrons to form a covalent bond.[82] Hence, the valence state of TMs would directly influence the bonding strength with the intermediates.

The valence state of different TM atoms is defined as the number of electrons transferred from the TM atom to the substrate. Using the valence state of TMs as the descriptor, we find that a volcano trend is observed for $TM@Ti_3C_2O_{2-x}B_x$ (Fig. 10a), meaning this descriptor is possible to estimate the catalytic performance of the $TM@Ti_3C_2O_2$ system. Therefore, a brief calculation of N-doped $Ti_3C_2O_2$-based SACs ($TM@Ti_3C_2O_{2-x}N_x$) is carried out to verify the accuracy of this descriptor. The adsorption configuration of $CO_2$ and CO on $TM@Ti_3C_2O_{2-x}N_x$ (Fig. S9, ESI†) indicates that the nitrogen atom is only used as the coordination atom to control the electronic structure of the TM. Generally, the potential-limiting step of $CO_2$ reduction is the hydrogenation of *COOH to *CO or the hydrogenation of *CO to *CHO.[83,84] As for the $TM@Ti_3C_2O_2$ system studied in our work, $*OH + H^+ + e^- \rightarrow H_2O(l)$ is the potential-limiting step on $V@Ti_3C_2O_2$ and $Cr@Ti_3C_2O_2$. Hence, we have calculated these key reaction steps on $TM@Ti_3C_2O_{2-x}N_x$ and chosen the step with the largest reaction energy barrier as the potential-limiting step.

The result shows that a volcano trend is observed with the optimal scope of the valence state ranging from ~0.8 e to ~1.1 e (Fig. 10b). We can see that the optimal scope of the valence state is different between $TM@Ti_3C_2O_{2-x}B_x$ and $TM@Ti_3C_2O_2$ ($TM@Ti_3C_2O_{2-x}B_x$). Because the boron atom can participate in $CO_2$ reduction, the scaling relations between the adsorption strength of reaction intermediates have been broken. This simple descriptor well explains the catalytic performance of the $TM@Ti_3C_2O_2$ and doped $TM@Ti_3C_2O_2$ SACs and suggests that a certain moderate degree of electron transfer from TM atoms to the substrate will be expected to promote the overall catalytic activity. Before using this descriptor, we need to determine whether the coordination atoms participate in the reaction to ensure that the same linear relationship exists. Moreover, this descriptor can only roughly estimate the $CO_2$RR performance of catalysts. A series of subsequent tests, such as the competition test, stability test and solvation effect should be considered to further screening out the most suitable catalysts.

## 4. Conclusions

In summary, by applying well-defined first-principles calculations, we have investigated the single-atom catalysts of $Ti_3C_2O_{2-x}B_x$ monolayers for $CO_2$ electrochemical reduction reactions. The results obtained suggest that the B atom not only serves as the coordination atom to anchor single TM atoms but also plays an important role in the $CO_2$ electrochemical reduction process. The strategy of doping B regulates the charge–orbit distribution of the surface functional groups of $Ti_3C_2O_2$. By analyzing charge transfer and DOS calculation results, the combined effect of the single TM atom and the adjacent B atom in $Ti_3C_2O_{2-x}B_x$ on the $CO_2$RR has been

demystified. The empty orbitals in B atom hybridization help it in gaining more electrons from single TM atoms, forming strong-polarized covalent TM–B bonds, which is beneficial for anchoring single TM atoms on the $Ti_3C_2O_2$ surface. The electrons provided by the occupied orbitals in B atom hybridization are effectively transferred to the π-antibonding orbitals of $CO_2$ and CO, thereby helping single TM atoms to activate the $CO_2$ molecules and *CO intermediate. Especially, the activation of the *CO intermediate induced by the combined effect effectively lowers the reaction energy barrier of the protonation step of *CO, facilitating further CO reduction towards $CH_4$.

Our results also demonstrated that the activated $CO_2$ can be further reduced to $CH_4$ by TM@$Ti_3C_2O_{2-x}B_x$, in which Fe@$Ti_3C_2O_{2-x}B_x$ exhibits a better catalytic efficiency with a low limiting potential of ~0.40 V. In addition, AIMD calculations reveal that Fe@$Ti_3C_2O_{2-x}B_x$ has a high stability. Inspired by the successful preparation of Ru@$Ti_3C_2O_{2-x}B_x$ SACs,[55] the practical application of Fe@$Ti_3C_2O_{2-x}B_x$ in $CO_2$ capture and reduction can be reasonably anticipated in the near future. We conclude that our work provides atomic-level insights into the combined effect between the embedded single metal atom and the innate atom in a substrate and provides an important strategy for the design of MXenes as novel $CO_2$RR catalysts.

## Conflicts of interest

There are no conflicts to declare.

## Acknowledgements

This work was supported by Guangdong Basic and Applied Basic Research Foundation (No. 2022A1515011303), the Central Government Guides Local Science and Technology Development Funds to Freely Explore Basic Research Projects (2021Szvup106), the Natural Science Fund for Distinguished Young Scholars of Hubei Province (No. 2020CFA087), the Basic Research Program of Shenzhen (No. JCYJ20190809120015163); and the Fundamental Research Funds for the Central Universities.

## References

1 Ş. Kılkış, G. Krajačić, N. Duić, M. A. Rosen and M. D. A. Al-Nimr, *Energy Convers. Manage.*, 2020, **225**, 113410.
2 D. Guan, J. Meng, D. M. Reiner, N. Zhang, Y. Shan, Z. Mi, S. Shao, Z. Liu, Q. Zhang and S. J. Davis, *Nat. Geosci.*, 2018, **11**, 551–555.
3 Z. Chu, M. Cheng and N. N. Yu, *Technol. Forecase. Soc.*, 2021, **172**, 121037.
4 X. Zhao, Y. Shang and M. Song, *Socio-Econ. Plan. Sci.*, 2020, **72**, 100757.
5 X. Zhao, X. Ma, B. Chen, Y. Shang and M. Song, *Resour., Conserv. Recycl.*, 2022, **176**, 105959.
6 M. Salvia, D. Reckien, F. Pietrapertosa, P. Eckersley, N.-A. Spyridaki, A. Krook-Riekkola, M. Olazabal, S. De Gregorio Hurtado, S. G. Simoes, D. Geneletti, V. Viguié, P. A. Fokaides, B. I. Ioannou, A. Flamos, M. S. Csete, A. Buzasi, H. Orru, C. de Boer, A. Foley, K. Rižnar, M. Matosović, M. V. Balzan, M. Smigaj, V. Baštáková, E. Streberova, N. B. Šel, L. Coste, L. Tardieu, C. Altenburg, E. K. Lorencová, K. Orru, A. Wejs, E. Feliu, J. M. Church, S. Grafakos, S. Vasilie, I. Paspaldzhiev and O. Heidrich, *Renewable Sustainable Energy Rev.*, 2021, **135**, 110253.
7 Z. Liu, Z. Deng, G. He, H. Wang, X. Zhang, J. Lin, Y. Qi and X. Liang, *Nat. Rev. Earth Environ.*, 2022, **3**, 141–155.
8 M. M. Ayyub and C. N. R. Rao, *Mater. Horiz.*, 2021, **8**, 2420–2443.
9 Z. Sun, T. Ma, H. Tao, Q. Fan and B. Han, *Chem*, 2017, **3**, 560–587.
10 L. Dietz, S. Piccinin and M. Maestri, *J. Phys. Chem. C*, 2015, **119**, 4959–4966.
11 X. Li, S. Wang, L. Li, X. Zu, Y. Sun and Y. Xie, *Acc. Chem. Res.*, 2020, **53**, 2964–2974.
12 D. W. DeWulf, T. Jin and A. J. Bard, *J. Electrochem. Soc.*, 1989, **136**, 1686.
13 Y. Hori, in *Modern Aspects of Electrochemistry*, ed. C. G. Vayenas, R. E. White and M. E. Gamboa-Aldeco, Springer New York, New York, NY, 2008, pp. 89–189, DOI: 10.1007/978-0-387-49489-0_3.
14 A. A. Peterson, F. Abild-Pedersen, F. Studt, J. Rossmeisl and J. K. Nørskov, *Energy Environ. Sci.*, 2010, **3**, 1311–1315.
15 W. Chen, J. Cao, W. Fu, J. Zhang, G. Qian, J. Yang, D. Chen, X. Zhou, W. Yuan and X. Duan, *Angew. Chem., Int. Ed.*, 2022, **61**, e202200190.
16 Y.-J. Zhang, V. Sethuraman, R. Michalsky and A. A. Peterson, *ACS Catal.*, 2014, **4**, 3742–3748.
17 X. Chen, L. P. Granda-Marulanda, I. T. McCrum and M. T. M. Koper, *Nat. Commun.*, 2022, **13**, 38.
18 J. Albo and A. Irabien, *J. Catal.*, 2016, **343**, 232–239.
19 I. Merino-Garcia, J. Albo, J. Solla-Gullón, V. Montiel and A. Irabien, *J. CO2 Util.*, 2019, **31**, 135–142.
20 Y. Hori, A. Murata and R. Takahashi, *J. Chem. Soc., Faraday Trans. 1*, 1989, **85**, 2309–2326.
21 J. Albo, G. Beobide, P. Castaño and A. Irabien, *J. CO2 Util.*, 2017, **18**, 164–172.
22 J. Albo, A. Sáez, J. Solla-Gullón, V. Montiel and A. Irabien, *Appl. Catal., B*, 2015, **176–177**, 709–717.
23 J. Albo, D. Vallejo, G. Beobide, O. Castillo, P. Castaño and A. Irabien, *ChemSusChem*, 2017, **10**, 1100–1109.
24 M. Perfecto-Irigaray, J. Albo, G. Beobide, O. Castillo, A. Irabien and S. Pérez-Yáñez, *RSC Adv.*, 2018, **8**, 21092–21099.
25 I. Merino-Garcia, J. Albo, P. Krzywda, G. Mul and A. Irabien, *Catal. Today*, 2020, **346**, 34–39.
26 Q. Zhang and J. Guan, *Adv. Funct. Mater.*, 2020, **30**, 2000768.
27 M. Li, H. Wang, W. Luo, P. C. Sherrell, J. Chen and J. Yang, *Adv. Mater.*, 2020, **32**, 2001848.
28 R. Wang, G. Liu, S. K. Kim, K. H. Bowen and X. Zhang, *J. Energy Chem.*, 2021, **63**, 130–137.
29 N. Li, X. Wang, X. Lu, P. Zhang and W.-J. Ong, *Chem. – Eur. J.*, 2021, **27**, 17900–17909.

 

30 J. Fu, L. Zhu, K. Jiang, K. Liu, Z. Wang, X. Qiu, H. Li, J. Hu, H. Pan, Y.-R. Lu, T.-S. Chan and M. Liu, *Chem. Eng. J.*, 2021, **415**, 128982.
31 C. Ling, X. Niu, Q. Li, A. Du and J. Wang, *J. Am. Chem. Soc.*, 2018, **140**, 14161–14168.
32 H. Yin, L.-Y. Gan and P. Wang, *J. Mater. Chem. A*, 2020, **8**, 3910–3917.
33 M.-A. Légaré, G. Bélanger-Chabot, R. D. Dewhurst, E. Welz, I. Krummenacher, B. Engels and H. Braunschweig, *Science*, 2018, **359**, 896–900.
34 M. Qu, G. Qin, J. Fan, A. Du and Q. Sun, *Appl. Surf. Sci.*, 2021, **555**, 149652.
35 Y. Jiao, A. Du, Z. Zhu, V. Rudolph, G. Q. Lu and S. C. Smith, *Catal. Today*, 2011, **175**, 271–275.
36 S. Tang, X. Zhou, S. Zhang, X. Li, T. Yang, W. Hu, J. Jiang and Y. Luo, *ACS Appl. Mater. Interfaces*, 2019, **11**, 906–915.
37 X. Chen, W.-J. Ong, X. Zhao, P. Zhang and N. Li, *J. Energy Chem.*, 2021, **58**, 577–585.
38 S. Liu, M. Jin, J. Sun, Y. Qin, S. Gao, Y. Chen, S. Zhang, J. Luo and X. Liu, *Chem. Eng. J.*, 2022, **437**, 135294.
39 H. Xu, Y. Zhao, Q. Wang, G. He and H. Chen, *Coord. Chem. Rev.*, 2022, **451**, 214261.
40 J. Li, Q. Guan, H. Wu, W. Liu, Y. Lin, Z. Sun, X. Ye, X. Zheng, H. Pan, J. Zhu, S. Chen, W. Zhang, S. Wei and J. Lu, *J. Am. Chem. Soc.*, 2019, **141**, 14515–14519.
41 N. Li, X. Chen, W.-J. Ong, D. R. MacFarlane, X. Zhao, A. K. Cheetham and C. Sun, *ACS Nano*, 2017, **11**, 10825–10833.
42 J. Peng, X. Chen, W.-J. Ong, X. Zhao and N. Li, *Chem*, 2019, **5**, 18–50.
43 R. A. Soomro, S. Jawaid, Q. Zhu, Z. Abbas and B. Xu, *Chin. Chem. Lett.*, 2020, **31**, 922–930.
44 Y. Dong, H. Shi and Z.-S. Wu, *Adv. Funct. Mater.*, 2020, **30**, 2000706.
45 B. Huang, N. Li, W.-J. Ong and N. Zhou, *J. Mater. Chem. A*, 2019, **7**, 27620–27631.
46 Y. Meng, J.-X. Liang, C. Zhu, C.-Q. Xu and J. Li, *Sci. China Mater.*, 2022, **65**, 1303–1312.
47 G. Chen, M. Ding, K. Zhang, Z. Shen, Y. Wang, J. Ma, A. Wang, Y. Li and H. Xu, *ChemSusChem*, 2022, **15**, e202102352.
48 M. Zhang, C. Lai, B. Li, S. Liu, D. Huang, F. Xu, X. Liu, L. Qin, Y. Fu, L. Li, H. Yi and L. Chen, *Small*, 2021, **17**, 2007113.
49 Y. Cui, Z. Cao, Y. Zhang, H. Chen, J. Gu, Z. Du, Y. Shi, B. Li and S. Yang, *Small Sci.*, 2021, **1**, 2100017.
50 D. Zhao, Z. Chen, W. Yang, S. Liu, X. Zhang, Y. Yu, W.-C. Cheong, L. Zheng, F. Ren, G. Ying, X. Cao, D. Wang, Q. Peng, G. Wang and C. Chen, *J. Am. Chem. Soc.*, 2019, **141**, 4086–4093.
51 Q. Zhao, C. Zhang, R. Hu, Z. Du, J. Gu, Y. Cui, X. Chen, W. Xu, Z. Cheng, S. Li, B. Li, Y. Liu, W. Chen, C. Liu, J. Shang, L. Song and S. Yang, *ACS Nano*, 2021, **15**, 4927–4936.
52 W. Lin, Y.-R. Lu, W. Peng, M. Luo, T.-S. Chan and Y. Tan, *J. Mater. Chem. A*, 2022, **10**, 9878–9885.
53 H. Liu, Z. Hu, Q. Liu, P. Sun, Y. Wang, S. Chou, Z. Hu and Z. Zhang, *J. Mater. Chem. A*, 2020, **8**, 24710–24717.
54 Z. Chen, J. Cao, X. Wu, D. Cai, M. Luo, S. Xing, X. Wen, Y. Chen, Y. Jin, D. Chen, Y. Cao, L. Wang, X. Xiong and B. Yu, *ACS Appl. Mater. Interfaces*, 2022, **14**, 12223–12233.
55 M. Bat-Erdene, M. Batmunkh, B. Sainbileg, M. Hayashi, A. S. R. Bati, J. Qin, H. Zhao, Y. L. Zhong and J. G. Shapter, *Small*, 2021, **17**, 2102218.
56 N. Li, J. Peng, Z. Shi, P. Zhang and X. Li, *Chin. J. Catal.*, 2022, **43**, 1906–1917.
57 J. Hafner, *J. Comput. Chem.*, 2008, **29**, 2044–2078.
58 J. P. Perdew, K. Burke and M. Ernzerhof, *Phys. Rev. Lett.*, 1996, **77**, 3865–3868.
59 P. E. Blöchl, *Phys. Rev. B: Condens. Matter Mater. Phys.*, 1994, **50**, 17953–17979.
60 S. Grimme, J. Antony, S. Ehrlich and H. Krieg, *J. Chem. Phys.*, 2010, **132**, 154104.
61 E. Sanville, S. D. Kenny, R. Smith and G. Henkelman, *J. Comput. Chem.*, 2007, **28**, 899–908.
62 K. Momma and F. Izumi, *J. Appl. Crystallogr.*, 2011, **44**, 1272–1276.
63 C. M. Gray, K. Saravanan, G. Wang and J. A. Keith, *Mol. Simul.*, 2017, **43**, 420–427.
64 F. Calle-Vallejo, R. F. de Morais, F. Illas, D. Loffreda and P. Sautet, *J. Phys. Chem. C*, 2019, **123**, 5578–5582.
65 Q. Zhang and A. Asthagiri, *Catal. Today*, 2019, **323**, 35–43.
66 L. Li, B. Li, Q. Guo and B. Li, *J. Phys. Chem. C*, 2019, **123**, 14501–14507.
67 H. Dong, C. Liu, Y. Li and D.-E. Jiang, *Nanoscale*, 2019, **11**, 11351–11359.
68 J. K. Nørskov, J. Rossmeisl, A. Logadottir, L. Lindqvist, J. R. Kitchin, T. Bligaard and H. Jónsson, *J. Phys. Chem. B*, 2004, **108**, 17886–17892.
69 F. Calle-Vallejo, J. I. Martínez, J. M. García-Lastra, M. Mogensen and J. Rossmeisl, *Angew. Chem., Int. Ed.*, 2010, **49**, 7699–7701.
70 Y. Li, H. Su, S. H. Chan and Q. Sun, *ACS Catal.*, 2015, **5**, 6658–6664.
71 D. R. Lide, *CRC handbook of chemistry and physics*, CRC Press, 2004.
72 Y. Gao, Y. Cao, Y. Gu, H. Zhuo, G. Zhuang, S. Deng, X. Zhong, Z. Wei, J. Chen, X. Pan and J.-G. Wang, *Appl. Surf. Sci.*, 2019, **465**, 911–918.
73 P. Li, J. Zhu, A. D. Handoko, R. Zhang, H. Wang, D. Legut, X. Wen, Z. Fu, Z. W. Seh and Q. Zhang, *J. Mater. Chem. A*, 2018, **6**, 4271–4278.
74 C. Guo, T. Zhang, X. Liang, X. Deng, W. Guo, Z. Wang, X. Lu and C.-M. L. Wu, *Appl. Surf. Sci.*, 2020, **533**, 147466.
75 X. Cui, W. An, X. Liu, H. Wang, Y. Men and J. Wang, *Nanoscale*, 2018, **10**, 15262–15272.
76 M. Wang, L. Kong, X. Lu and C.-M. Lawrence Wu, *J. Mater. Chem. A*, 2022, **10**, 9048–9058.
77 T. Liu, G. Wang and X. Bao, *J. Phys. Chem. C*, 2021, **125**, 26013–26020.

78 A. Föhlisch, M. Nyberg, P. Bennich, L. Triguero, J. Hasselström, O. Karis, L. G. M. Pettersson and A. Nilsson, *J. Chem. Phys.*, 2000, **112**, 1946–1958.
79 K. M. Gameel, I. M. Sharafeldin, A. U. Abourayya, A. H. Biby and N. K. Allam, *Phys. Chem. Chem. Phys.*, 2018, **20**, 25892–25900.
80 X. Hong, K. Chan, C. Tsai and J. K. Nørskov, *ACS Catal.*, 2016, **6**, 4428–4437.
81 S. Zheng, C. Zuo, X. Liang, S. Li and F. Pan, *J. Energy Chem.*, 2021, **56**, 444–448.
82 L. Gong, D. Zhang, C.-Y. Lin, Y. Zhu, Y. Shen, J. Zhang, X. Han, L. Zhang and Z. Xia, *Adv. Energy Mater.*, 2019, **9**, 1902625.
83 Y. Ouyang, L. Shi, X. Bai, Q. Li and J. Wang, *Chem. Sci.*, 2020, **11**, 1807–1813.
84 C. Li, X. Liu, F. Xu, D. Wu, H. Xu and G. Fan, *Electrochim. Acta*, 2022, **426**, 140764.



 